Methane steam reforming reaction in solid oxide fuel cells

Fan, Liyuan; Mokhov, Anatoli; Saadabadi, S. Ali; Brandon, Nigel; Aravind, Purushothaman Vellayani

IMPORTANT NOTE: You are advised to consult the publisher's version (publisher's PDF) if you wish to cite from it. Please check the document version below.

Document Version
Publisher's PDF, also known as Version of record

Publication date:
2021

[Link to publication in University of Groningen/UMCG research database](#)

Methane steam reforming reaction in solid oxide fuel cells: Influence of electrochemical reaction and anode thickness

Liyuan Fan [a,*], Anatoli Mokhov [b], S. Ali Saadabadi [c], Nigel Brandon [d], Purushothaman Vellayani Aravind [b]

[a] College of Science and Engineering, James Cook University, 1 James Cook Drive, Townsville QLD 4811, Australia
[b] Energy and Sustainability Research Institute Groningen, University of Groningen, Groningen, 9700 AB, The Netherlands
[c] Process & Energy, 3mE, Leeghwaterstraat 39, Delft University of Technology, Delft, 2628 CB, The Netherlands
[d] Department of Earth Science & Engineering, Faculty of Engineering, Imperial College London, South Kensington Campus, London SW7 2AZ, UK

HIGHLIGHTS

- Current promotes the methane steam reforming reaction rate.
- Anode thickness influences the fitted activation energy.
- More experimental data is helpful in getting a reliable rate expression.
- Importance of studying effect of mass-transfer on the global MSR kinetics.

GRAPHICAL ABSTRACT
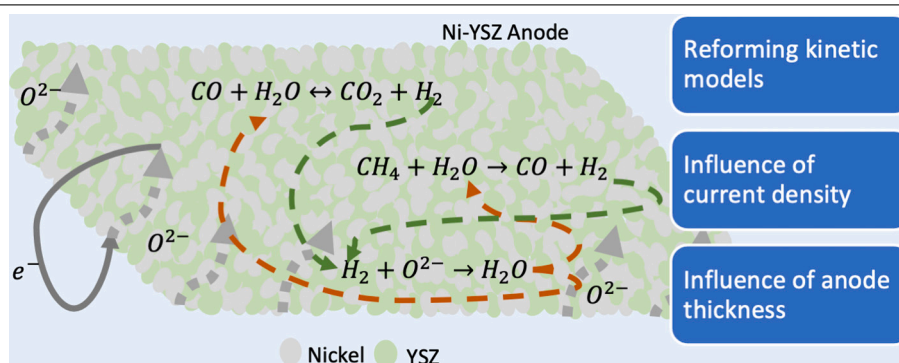
ARTICLE INFO

ABSTRACT

The influence of operation temperature, inlet gas composition, current density and the anode thickness on the methane steam reforming reaction over nickel yttria-stabilized zirconia anodes was experimentally studied in solid oxide fuel cells. The experimental results were analyzed using data fitting in Power-Law and Langmuir–Hinshelwood kinetic models. Similar trends of dependence of methane and steam partial pressures were observed in both models. The methane reaction order is positive. Negative influence of steam partial pressure on the methane steam reforming reaction rate are found. The electrochemical reaction and anode thickness affect the reforming kinetics parameters. The anodes thickness shows particular influences on the steam reaction order, and the activation energy when a current is produced. The model evaluation suggests that the two models are comparable and the extra parameters within the Langmuir–Hinshelwood kinetic model are contributing to the lower mean absolute percentage error and higher coefficient of determination R^2.

1. Introduction

Nickel is well known for its catalytic ability of reforming CH_4, and nickel-based materials have been widely used as anode materials in Solid Oxide Fuel Cells (SOFCs) due to their large number of catalytic active sites [1–9]. Natural gas or biosyngas containing CH_4 can therefore be potentially used in SOFCs directly as fuels without external

---

* Corresponding author.
  E-mail address: liyuan.fan@jcu.edu.au (L. Fan).

**Nomenclature**

n	Amount of gas, mole
AIC	Akaike Information Criterion
BIC	Bayesian Information Criterion
MSR	Methane Steam Reforming
Ni-GDC	Nickel-Gadolinium Doped Ceria
Ni-YSZ	Nickel yttria-stabilized zirconia
SOFC	Solid Oxide Fuel Cell
$\triangle H_j^0$	Change of adsorption enthalpy of species j.
$\triangle S_j^0$	Change of entropy of species j.
$\triangle G_{msr}^0$	Change of the standard Gibbs free energy of the MSR reaction
$\triangle G_{wgs}^0$	Change of the standard Gibbs free energy of the WGS reaction
$\triangle H_{298}$	Reaction heat
a	Reaction order of methane
A_{CH_4}	Pre-exponential factors of the adsorption constant for methane
A_{H_2O}	Pre-exponential factors of the adsorption constant for steam
α	Reaction order, dimensionless coefficients
α_{CH_4}	Reaction order of methane
α_{H_2O}	Reaction order of steam
b	Reaction order of steam
β	Driving force
c	Reaction order of hydrogen
E_a	Activation energy
F	Faraday constant
F_{CH_4}	Methane molar flow rate, mol/s
k	Reaction rate constant
k_0	Pre-exponential factor
K_{CH_4}	Adsorption constant of methane.
K_{CO}	Adsorption constant of carbon monoxide.
$K_{eq,msr}$	Equilibrium constant of methane steam reforming reaction
$K_{eq,msr}$	Equilibrium constant for MSR reaction
$K_{eq,wgs}$	Equilibrium constant of water gas shift reaction
K_{H_2O}	Adsorption constant of steam.
K_{H_2}	Adsorption constant of hydrogen.
K_j	adsorption coefficient of species j
$M_{CH_4}^{outlet}$	Methane flowrate at the outlet
$M_{CH_4}^{outlet}$	Methane molecular weight, g/mol
$M_{N_2}^{outlet}$	Nitrogen flowrate at the outlet
P	Total pressure, 1 bar
p	Partial pressure , bar
R	Universal gas constant, 8.314 J/(mol K)

|	
r_{CH_4}	Reforming rate of MSR, mol/(s g)
T	Temperature, K
w_{cat}	Total weight of the catalyst, g
$W_{N_2}^{outlet}$	Nitrogen molecular weight, g/mol
X_{CH_4}	Methane fractional conversion
x_{CH_4}	Overall methane conversion
CC	Current to Carbon Ratio
DC	Carbon dioxide to carbon ratio
HC	Hydrogen to Carbon ratio
NC	Nitrogen to Carbon ratio
SC	Steam to Carbon ratio

The electrochemical reactions of H_2 is strongly exothermic, and the heat produced by the electrochemical reactions helps promote the overall endothermic MSR-WGS reactions [15,16]. The direct internal reforming makes the SOFC systems more efficient and cost-effective [17]. Studies of MSR reactions have been widely conducted during the last decades, and most were conducted on nickel-based catalytic materials with appropriate ranges of temperature and steam to carbon ratio for safe operations [1,18–25]. These studies yielded various CH_4 reaction orders and activation energies varying from 19 kJ/mol to 240 kJ/mol [1,21,26]. However, no correlation between anode thickness and the catalytic activity have been reported. In addition, the interaction of the electrochemical reactions and the reforming reaction is essential in understanding the influence of the current density on the catalytic activity. The authors of this study have reported that the electrochemical reaction has a slightly positive influence on the MSR reaction rate on Nickel-Gadolinium Doped Ceria (Ni-GDC) anodes [27]. Thallam Thattai et al. have reported a large dependence of the reaction orders in the Power-Law kinetic model and exponents in the Langmuir–Hinshelwood kinetic model on the local current density, and both kinetic models show that the electrochemical reaction promotes the MSR reaction [28]. Nakagawa et al. have reported a catalytic activity deterioration with a current density as high as 6000 A/m^2 in direct internal reforming SOFCs [26]. These results are contradicting, and therefore needs further investigations.

Methane reforming in the presence of catalyst is a very complex multi-step chemical process including both gas phase and surface reactions which strongly depend upon operation conditions. There is no one comprehensive rate expression for MSR reaction rates. The rates of elementary steps are either known with very low accuracy or completely unknown. Thus the MSR reaction rate cannot be derived using the rates of elementary steps. Various approximations are made including single layer adsorption, no diffusion limitation, and only the reactants influence the reaction rates [2,10,24,26,29–32]. The proposed rate expressions vary among various kinetic models including First-Order [21,24,33,34], Power-Law [18–20,25,27–29,35–40], Langmuir–Hinshelwood [1,28,38,41], and Langmuir–Hinshelwood–Hougen–Watson [22,38]. The authors of this paper have conducted modeling studies using the most widely used rate expression, the Power-Law expression reported by Achenbach and Riensche [15,16,18]. However, the nickel content (20 wt%) was lower than the typical amount used in SOFC anodes (50–70 wt%). Moreover, due to unmatchable operation conditions such as the anode thickness and the feed gas compositions, the experimental data observed in the study cannot be directly used in other studies. Another rate expression used by Lehnert et al. was reported by Xu and Froment on an industrial type of catalyst, where a first-order dependence of both methane and steam concentrations were assumed [1,42]. However, the latter is rarely experimentally observed, especially at conditions relevant for direct internal MSR in SOFCs. Thallam Thattai et al. have also pointed out the insufficient research on MSR global and intrinsic kinetics on complete anodes which emphasized the need to develop readily applicable global kinetic models for SOFCs

reformers. Internal reforming can be carried out in SOFCs directly with various reforming agents [10–14]. As the most commonly used reforming agent, steam could reform CH_4 into a mixture of H_2 and CO in the Methane Steam Reforming (MSR) reaction:

$$CH_4 + H_2O \longleftrightarrow CO + 3H_2, \quad \triangle H_{298} = +206 \text{ kJ/mol} \tag{1}$$
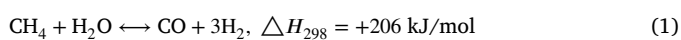
The produced CO can further react via the Water Gas Shift (WGS) reaction:

$$CO + H_2O \longleftrightarrow CO_2 + H_2, \quad \triangle H_{298} = -41 \text{ kJ/mol} \tag{2}$$
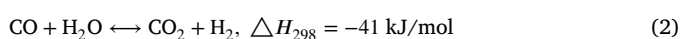
under operation conditions. They identified the limitations of using the previously proposed rate expressions for Ni based catalyst beds to study MSR kinetics for complete cermet anodes in SOFCs [27,28,38,43]. In their study, the Power-Law and Langmuir–Hinshelwood kinetic models were used and predicted significantly different local MSR reaction rates and species distributions along the normalized channel on Ni-GDC anodes which is an indication for a need of further study. The present work is therefore the extension of this study. The operation conditions including the flow rate, gas composition, temperature, current density, the material and dimension of the anode were different from their study. Our goal in this study was to analyze the influence of electrochemical reaction and anode thickness on the global reforming kinetic parameters over Nickel Yttria-Stabilized Zirconia (Ni-YSZ) anodes in SOFCs to get reliable rate expressions for future SOFC modeling studies. Towards this aim, the MSR reaction rates were measured under various operation conditions which were then analyzed using the Power-Law and Langmuir–Hinshelwood kinetic models. These two kinetic models were then compared and evaluated. These results can also provide insights on the anode design and SOFC operation condition optimization in the future modeling studies [3,11,13–17,44].

2. Experiment

2.1. Cermet anode ink preparation

NiO-YSZ (62.5 : 37.5) powder was purchased from Nextech Fuel Cell Materials. The anode composite powder and the dispersant (Hypermer KD15) were thoroughly mixed using a planetary ball mill (Retsch PM 100, Germany) with isopropanol for one hour. The ball milling media consisted of ZrO_2 (Tosoh Co., Japan) balls (3 mm in diameter) and a Zirconia bowl (250 cm^3). The ball to powder ratio was 4 to 1, and the rotation speed was 200 rpm. After milling, the wet ball-milled powders were dried in an oven at 360 K for 24 h. This powder was then mixed with terpineol and an ethylcellulose binder. The cermet powders' solid loading was 75 wt% of the final inks, which contained 2.5 mg/m^2 dispersant calculated based on the cermet powders' specific surface area. The amount of binder used in this preparation was 3 wt% of the cermet powder. The mixture was homogenized using a triple roll mill (EXAKT 80E, Germany).

2.2. SOFC button cell preparation

In this study, experiments have been carried out using electrolyte supported button cells which were produced using 150 μm YSZ electrolytes (Fuel Cell Materials). First, a GDC ink was printed on the cathode side to work as an inter-layer and fired at 1573 K. Next, the anode ink was screen printed onto the anode side of YSZ pellets as shown in Fig. 1(a). The thickness of the anode was controlled by either screen printing a single anode layer, or printing once, drying at 360 K, then screen printing a second anode layer on top of the first. This was repeated as many times as needed to create an anode of the desired thickness. After printing, the pellets were dried and then fired at 1573 K for one hour. The circular anode surface area was 0.95 cm^2. The cathode (counter electrode) was also a circular with the same diameter as the anode. The reference electrode was coaxial to the counter electrode. A diagram of the sample is shown in Fig. 1(b). The geometric area of the anode was 0.95 cm^2. After reduction, the anode thicknesses were determined using SEM. The nickel content was 57 wt%. Two anode configurations were used to investigate the influence of anode thickness on the kinetic activities, anode A with a thickness of 16 μm and anode B with a thickness of 27 μm, and the total weight of anode materials for anode A and B were 8.5 mg and 14.3 mg, respectively.

The button cell was attached to an alumina tube using Aron ceramic paste (Aremco, USA). Fuel gas was supplied through a narrower alumina tube directly to the anode inside the larger tube, as shown

Table 1
Molar fractions (in %) of the inlet fuel, and the total flow-rate is 100 ml/min.

Case No.	CH_4	H_2	H_2O	N_2
i	4	5	22	69
ii	8	5	22	65
iii	12	5	22	61
iv	8	5	19	68
v	8	5	16	71

in Fig. 1(c). The cathode was open to ambient air, and the oxygen depletion was negligible for the experiment's duration. A diluted silver paste was applied to the electrode surface to act as a current collector. Silver wire was used for electrical contact, which was attached to the electrodes with silver paste. The cell temperature was monitored with a type K thermocouple positioned about 5 mm above the counter electrode's surface. The cell was taken up to an operating temperature of 1073 K at a ramp rate of 2 K/min with the anode side exposed to an inert atmosphere of nitrogen. The anode was reduced at 1073 K by increasing the hydrogen partial pressure stepwise: 5.0% (30 min), 10% (90 min). During reduction, gases were passed through a water bubbler in a temperature-controlled water bath to achieve 2% humidification.

2.3. Measuring procedure

The experiments were performed when the furnace temperature was gradually decreased from 1048 K to 973 K at the rate of 2 K/min. The current density was set at 0, 632 and 1052 A/m^2 under galvanostatic conditions by using an Autolab PGSTAT302 (Eco Chemie) current controller. During the measurements, deionized water was added to the heated line carrying fuel gases by using a syringe pump to generate steam. Steam mole fraction in the inlet gas flow was in the range from 16% to 22% to avoid carbon deposition. No degradation of the catalyst was expected. The inlet gas flows to the fuel cell were set by mass flow controllers (Bronkhorst Thermo) shown in Fig. 1(c). The mass flow controllers were calibrated before use by using the same gas. Magnitudes of flow rates were always above 50% of full scales of the mass flow controllers that provided accuracy in measured flows better than 1%. The total gas flow rate at inlet was set to be 0.100 standard 100 ml/min (at $T = 273$ K and $P = 1$ bar). The gas compositions for 5 different cases are presented in Table 1. A sampling probe has been installed in the gas outlet. The sampled gas passed through an absorbent to remove water before entering a mass spectrometer (Prolab, Thermo Fisher) for gas composition analysis. The Mass Spectrometer was calibrated using gases with known composition. The accuracy of measuring CH_4 and N_2 mole fractions is estimated to be 2%.

3. Kinetic models

To evaluate the influence of operating conditions on the MSR reaction rates in direct internal reforming SOFCs, a reliable kinetic model is required. Two kinetic models, the Power-Law and the Langmuir–Hinshelwood kinetic models which are the most commonly used in SOFC modeling studies been chosen to investigate the influence of the electrochemical reaction and the anode thickness on the reforming kinetic parameters [1,18–20,25,27,28,28,29,35–38,38–41]. A Matlab script has been developed to calculate the kinetic parameters for both models.

X_{CH_4} is the CH_4 fractional conversion which is important for the investigation of the broad range of operation conditions on the MSR rates in SOFCs, and is calculated by:

$$X_{CH_4} = \frac{F_{CH_4}^{inlet} - F_{CH_4}(z_{cat})}{F_{CH_4}^{inlet}} \tag{3}$$
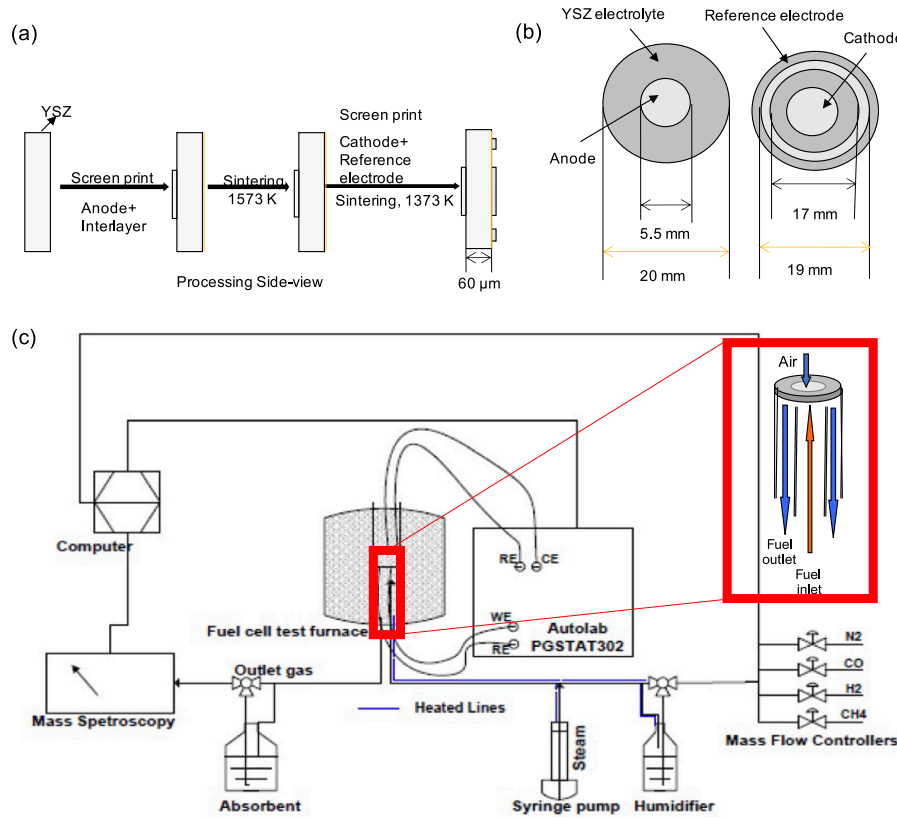
Fig. 1. Schematic illustration of (a) the button fuel cell fabrication process (not to scale); (b) the button fuel cell dimension (not to scale); and (c) the experiment test station (not to scale) including the furnace, the fuel cell test-rig, the mass spectrometer, the current collector, the computer, the mass flow controllers, the pre-treatment and post-treatment facilities of the fuel gas.

where $F_{CH_4}^{inlet}$ and $F_{CH_4}(z_{cat})$ are the CH_4 flow-rate at the inlet and z_{cat}, respectively. The overall CH_4 conversion x_{CH_4} at the exit is then calculated by:

$$x_{CH_4} = \frac{F_{CH_4}^{inlet} - F_{CH_4}^{outlet}}{F_{CH_4}^{inlet}} \tag{4}$$

where $F_{CH_4}^{outlet}$ is the CH_4 flow-rate at the outlet. N_2 is used as an inert gas flowing through the fuel cell, and assuming ideal gas behavior at constant pressure, $F_{CH_4}^{outlet}$ is calculated by:

$$F_{CH_4}^{outlet} = \frac{M_{CH_4}^{outlet}/W_{CH_4}}{M_{N_2}^{outlet}/W_{N_2}} \times F_{N_2}^{inlet} \tag{5}$$

where $F_{N_2}^{inlet}$ is the N_2 flow-rate at the inlet, regulated by the mass flow controller. $M_{CH_4}^{outlet}$ and $M_{N_2}^{outlet}$ are the CH_4 and N_2 flow-rates at the outlet measured by the mass spectrometer. W_{CH_4} and W_{N_2} are the CH_4 and N_2 molecular weights. The outlet overall CH_4 conversions with various inlet gas compositions at different temperatures are listed in Table 2.

3.1. Ideal plug flow reactor assumption

Given the relatively narrow porous paths in the SOFC anodes and low back mixing, a plug-flow reactor is assumed. Considering the total mass of catalyst w_{cat} in the SOFC as the equivalent to the total length of a plug-flow reactor, the mole balance under steady-state across a small catalyst element $\triangle W_{cat}$ is:

$$F_{CH_4}(W_{cat}) - F_{CH_4}(W_{cat} + \triangle W_{cat}) + r_{CH_4} \cdot \triangle W_{cat} = 0 \tag{6}$$

where r_{CH_4} is the MSR reaction rate, $F_{CH_4}(W_{cat})$ and $F_{CH_4}(W_{cat} + \triangle W_{cat})$ are the CH_4 flow-rates at (W_{cat}) and $(W_{cat} + \triangle W_{cat})$, respectively. If

Table 2
Overall methane conversions under different operation conditions. The temperature ranges from 973 K to 1048 K, and the current density varies from 0 to 1052 A/m².

Anode, Thickness	Temperature [K], Current density [A/m²]	Overall methane conversion (x_{CH_4})				
		i	ii	iii	iv	v
A, 16 μm	973, 0	0.212	0.142	0.090	0.225	0.234
	973, 632	0.245	0.193	0.174	0.226	0.246
	973, 1052	0.255	0.201	0.177	0.238	0.255
	998, 0	0.238	0.170	0.125	0.256	0.269
	998, 632	0.308	0.229	0.206	0.275	0.280
	998, 1052	0.322	0.239	0.217	0.277	0.288
	1023, 0	0.287	0.206	0.184	0.283	0.300
	1023, 632	0.363	0.265	0.239	0.304	0.327
	1023, 1052	0.381	0.280	0.249	0.321	0.325
	1048, 0	0.314	0.272	0.248	0.316	0.329
	1048, 632	0.399	0.293	0.265	0.335	0.367
	1048, 1052	0.415	0.308	0.309	0.356	0.362
B, 27 μm	973, 0	0.205	0.197	0.165	0.210	0.207
	973, 632	0.344	0.258	0.236	0.266	0.284
	9738, 1052	0.367	0.265	0.229	0.285	0.240
	1023, 0	0.314	0.276	0.219	0.262	0.260
	1023, 632	0.382	0.296	0.270	0.299	0.317
	1023, 1052	0.407	0.301	0.271	0.317	0.313
	1048, 0	0.428	0.305	0.253	0.296	0.290
	1048, 632	0.445	0.336	0.310	0.345	0.363
	1048, 1052	0.470	0.355	0.312	0.354	0.346

$\triangle W_{cat}$ becomes infinitely small, we get:

$$F_{CH_4}^{inlet} \cdot \int_0^{x_{CH_4}} dX_{CH_4} = \int_0^{w_{cat}} r_{CH_4} \cdot dW_{cat} \tag{7}$$

The inlet gas flow-rates provided were much higher than needed, and therefore a non-equilibrium status in the SOFC is assumed. Two reforming reaction rate expressions are used in Sections 3.2 and 3.3.

3.2. Power-law kinetic model

Reforming of methane occurs following a very complicated mechanism which is still not well known. The MSR reaction rate, especially in industrial field is approximated by Power-Law dependence:

$$r_{CH_4} = k \cdot p_{CH_4}^{\alpha_{CH_4}} \cdot p_{H_2O}^{\alpha_{H_2O}} \tag{8}$$

where p_{CH_4} and p_{H_2O} are the partial pressures of methane and steam, α_{CH_4} and α_{H_2O} are the reaction orders of methane and steam, respectively. The Power-Law kinetic model which has been intensively studied previously provides a straightforward and convenient method to describe the reaction rate without considering the complex surface chemistry [13,18–20,27–29,35–40,45–49]. The reaction orders can take any value, with −2.0 to 2.0 being a common range according to previously published data [18–20,25,27–29,35–40].

If we combine Eqs. (7) and (8), we get:

$$k = (\frac{F_{CH_4}^{inlet}}{w_{cat}}) \cdot \int_0^{x_{CH_4}} (\frac{1}{(p_{CH_4})^{\alpha_{CH_4}} (p_{H_2O})^{\alpha_{H_2O}}}) \cdot dX_{CH_4} \tag{9}$$

The electrochemical oxidation of H_2 occurs at the triple-phase boundary (TPB, gas/liquid/electron) where steam is also produced. Under closed-circuit operation, the direct methane oxidation and CO oxidation are very slow compared with the MSR reaction, and therefore neglected [27]. The current represents the electron flow-rate which can be expressed by the reaction rate according to the Faraday's law, and CC is the current to carbon ratio:

$$CC = \frac{i_{ele}}{2F \cdot F_{CH_4}^{inlet} \cdot X_{CH_4}} \tag{10}$$

where i_{ele} is the current in Ampere (A) and F is the Faraday's constant. The current influences the local gas partial pressures at the TPB. Here we also define SC as the steam to carbon ratio, NC as the nitrogen to carbon ratio, HC as the hydrogen to carbon ratio and DC as the carbon dioxide to carbon ratio. The partial pressure of different species in an SOFC can be calculated as follows:

$$p_{CH_4} = (\frac{n_{CH_4}}{n_{all}}) \cdot P = [\frac{(1 - X_{CH_4})}{(1 + SC + NC + HC + 2X_{CH_4})}] \cdot P \tag{11}$$

$$p_{H_2O} = (\frac{n_{H_2O}}{n_{all}}) \cdot P = [\frac{(SC - X_{CH_4} - DC + CC \cdot X_{CH_4})}{(1 + SC + NC + HC + 2X_{CH_4})}] \cdot P \tag{12}$$

$$p_{H_2} = (\frac{n_{H_2}}{n_{all}}) \cdot P = [\frac{(HC + 3X_{CH_4} + DC - CC \cdot X_{CH_4})}{(1 + SC + NC + HC + 2X_{CH_4})}] \cdot P \tag{13}$$

$$p_{CO} = (\frac{n_{CO}}{n_{all}}) \cdot P = [\frac{(X_{CH_4} - DC)}{(1 + SC + NC + HC + 2X_{CH_4})}] \cdot P \tag{14}$$

$$p_{CO_2} = (\frac{n_{CO_2}}{n_{all}}) \cdot P = [\frac{DC}{(1 + SC + NC + HC + 2X_{CH_4})}] \cdot P \tag{15}$$

where n_{all} is the total amount of the gas, and n_j is the amount of species j in the SOFC. A constant total pressure ($P = 1$ bar) is assumed. The WGS reaction is generally assumed to be at equilibrium because the rate constant of this reaction is large at moderate temperatures [1,50,51]. The equilibrium constant $K_{eq,wgs}$ can be calculated as:

$$K_{eq,wgs} = \frac{p_{CO_2} \cdot p_{H_2}}{p_{CO} \cdot p_{H_2O}} = \frac{DC \cdot (HC + 3X_{CH_4} + DC - CC \cdot X_{CH_4})}{(X_{CH_4} - DC) \cdot (SC - X_{CH_4} - DC + CC \cdot X_{CH_4})} \tag{16}$$

$$K_{eq,wgs} = \exp(- \triangle G_{wgs}^0/(R \cdot T)) \tag{17}$$

where $\triangle G_{wgs}^0$ is the change of the standard Gibbs free energy of the WGS reaction in J/mol. A temperature fitted empirical equation for the

equilibrium constant $K_{eq,wgs}$ previously reported by Mendez et al. [52] was implemented in this study:

$$K_{eq,wgs} = \exp(4577.8/T - 4.33) \tag{18}$$

The reforming reaction rate constant k in an SOFC can be then expressed as:

$$k = (\frac{F_{CH_4}^{inlet}}{w_{cat}}) \cdot$$
$$\int_0^{x_{CH_4}} \frac{1}{p^{(\alpha_{CH_4} + \alpha_{H_2O})} \cdot (1 - X_{CH_4})^{\alpha_{CH_4}}}$$
$$\cdot [\frac{(1 + SC + NC + HC + 2X_{CH_4})^{(\alpha_{CH_4} + \alpha_{H_2O})}}{(SC - X_{CH_4} - DC + CC \cdot X_{CH_4})^{\alpha_{H_2O}}}]$$
$$\cdot dX_{CH_4} \tag{19}$$

3.3. Langmuir-Hinshelwood kinetic model

The MSR catalytic reaction mechanism involves a sequence of elementary reaction steps. These steps involve the adsorption and desorption of reactants, products and intermediate species on the active catalytic sites [53]. The Langmuir–Hinshelwood Kinetic Model are commonly used to describe the surface chemistry of the catalytic reactions [29,34,38,41]. The expression of the reaction rate assumes that all species are chemisorbed and accommodated on the catalyst surface to react [28]. A general form of the rate expression for a heterocatalytic reaction could be then written as:

$$r = \frac{(\text{kinetic factor}) \cdot (\text{driving force})}{(\text{adsorption isotherm})} \tag{20}$$

where the kinetic factor describes the dependency of the reaction rate on the gas species involved in the rate-determining step, the adsorption isotherm accounts for the available active catalytic sites. The driving force reflects the equilibrium of the reaction. In the MSR reaction, assuming a single layer surface heterocatalytic reaction, the equilibrium constant $K_{eq,msr}$ could be expressed as:

$$K_{eq,msr} = \frac{p_{CO} \cdot p_{H_2}^3}{p_{CH_4} \cdot p_{H_2O}} \tag{21}$$

The equilibrium constant $K_{eq,msr}$ is also a function of temperature:

$$K_{eq,msr} = \exp(- \triangle G_{msr}^0/(R \cdot T))$$

where $\triangle G_{msr}^0$ is the change of Gibbs free energy of the MSR reaction. $K_{eq,msr}$ could be also calculated using an empirical equation [1,20]:

$$K_{eq,msr} = [\exp(-26830/T + 30.114)] \times 10^{-2} \tag{22}$$

The driving force β is calculated by [28,43,52]:

$$\beta = 1 - \frac{p_{CO} \cdot p_{H_2}^3}{K_{eq,msr} \cdot p_{CH_4} \cdot p_{H_2O}} \tag{23}$$

Xu et al. have proposed a Langmuir–Hinshelwood rate expression for the MSR reaction rate on a Ni–MgAl$_2$O$_4$ catalyst which has been widely used in modeling and experimental studies [13,15,16,20,28, 38,45,54]. The first-order dependence on methane partial pressure is a recurring result from the literature and is consistent with the most generally accepted rate determine step for the MSR reaction, methane chemisorption [1,18,20,25,26,28,34,35,38,41,55]. However, the dependence of methane partial has been also reported with various numbers ranging from 0.15 to1.4 [27–29,38]. Therefore a Langmuir–Hinshelwood rate equation including variable dependence of methane partial pressure has been used in this study [1,20,24,28,38]:

$$r_{CH_4} = \frac{kp_{CH_4}^a \cdot p_{H_2O}^b \cdot p_{H_2}^c (1 - \frac{p_{CO} \cdot p_{H_2}^3}{K_{eq,msr} \cdot p_{CH_4} \cdot p_{H_2O}})}{(1 + K_{CO}p_{CO} + K_{H_2}p_{H_2} + K_{CH_4}p_{CH_4} + K_{H_2O}p_{H_2O}/p_{H_2})^2} \tag{24}$$

where K_{CO}, K_{H_2}, K_{CH_4} and K_{H_2O} are the adsorption coefficients of CO, H_2, CH_4, and H_2O, respectively.

Table 3

Adsorption parameters for the Langmuir–Hinshelwood kinetic model. The temperature ranges from 973 K to 1048 K, and the current density varies from 0 to 1052 A/m².

Anode A and B Current density [A/m²]	Temperature (K)	K_{CH_4}	$\triangle H^0_{CH_4}$ (kJ/mol)	A_{CH_4}	$\triangle S^0_{CH_4}$ (J/(mol K))
0, 632, 1052	973	0.0755	−38.28	6.65e−4	−60.82
	998	0.0671			
	1023	0.0599			
	1048	0.0538			
Anode A, 16 μm Current density [A/m²]	**Temperature (K)**	K_{H_2O}	$\triangle H^0_{H_2O}$ (kJ/mol)	A_{H_2O}	$\triangle S^0_{H_2O}$ (J/(mol K))
0	973	0.0656	−38.98	5.30e−04	−62.71
	998	0.0582			
	1023	0.0519			
	1048	0.0465			
632	973	0.0327	−53.37	4.60e−05	−83.30
	998	0.0277			
	1023	0.0237			
	1048	0.0204			
1052	973	0.0408	−45.93	1.40e−04	−73.80
	998	0.0354			
	1023	0.0309			
	1048	0.0272			
Anode B, 27 μm Current density [A/m²]	**Temperature (K)**	K_{H_2O}	$\triangle H^0_{H_2O}$ (kJ/mol)	A_{H_2O}	$\triangle S^0_{H_2O}$ (J/(mol K))
0	973	0.0105	−35.31	1.33e−04	−74.20
	1023	0.0085			
	1048	0.0077			
632	973	0.0348	−39.68	2.58e−04	−68.70
	1023	0.0274			
	1048	0.0245			
1052	973	0.0148	−34.69	2.03e−04	−70.68
	1023	0.0120			
	1048	0.0109			

3.3.1. Parameter estimation and model simplification

During the experiments, the partial pressure of CO was low in the SOFCs, and the H_2 adsorption coefficient is very small due to the high temperature used [20,52]. The terms of $K_{CO}p_{CO}$ and $K_{H_2}p_{H_2}$ could then be estimated to be minimal, and thus be eliminated from the rate expression. The Langmuir–Hinshelwood rate expression can be further simplified as:

$$r_{CH_4} = \frac{k p^a_{CH_4} \cdot p^b_{H_2O} \cdot p^c_{H_2} (1 - \frac{p_{CO} \cdot p^3_{H_2}}{K_{eq,msr} \cdot p_{CH_4} \cdot p_{H_2O}})}{(1 + K_{CH_4}p_{CH_4} + K_{H_2O}p_{H_2O}/p_{H_2})^2} \tag{25}$$

The adsorption coefficient K_j could be calculated using van't Hoff equation:

$$K_j = \exp(-\frac{\triangle G^0_j}{RT}) = A_j \cdot \exp(-\frac{\triangle H^0_j}{RT}) \tag{26}$$

where A_j is the pre-exponential factor of the adsorption constant, $\triangle G^0_j$ is the change of Gibbs free energy, and $\triangle H^0_j$ is the change of adsorption enthalpy, of species j, respectively. $\triangle H^0_{CH_4} = -38.28$ kJ/mol and $A_{CH_4} = 6.65 \times 10^{-4}$ on Ni–MgAl$_2$O$_4$ catalyst have been reported and used by Elnashaie et al. on the same materials and van Biert et al. on Ni – GDC anodes [1,20,28], and were also implemented in this study. In an equilibrium adsorption process, the change of Gibbs free energy can be calculated by:

$$\triangle G^0_j = \triangle H^0_j - T \triangle S^0_j \tag{27}$$

The adsorption pre-exponential factors A_j can be calculated by [53]:

$$A_j = \exp(\frac{\triangle S^0_j}{R}) \tag{28}$$

where $\triangle S^0_j$ is the entropy change. The values for the adsorption parameters need to meet several thermodynamic criteria [1,28,38]:

1. adsorption is exothermic, and a negative adsorption enthalpy change ($\triangle H^0_j < 0$ kJ/mol) is required.
2. the entropy S would decrease after adsorption, and therefore $\triangle S^0_j < 0$ and $0 < A_j = \exp(\triangle S^0_j/R) < 1$.
3. Usually, the absolute values of entropy changes $\left|\triangle S^0_j\right|$ should be larger than 42 J/(mol K) which further narrows the values to $\triangle S^0_j < -42$ J/(mol K), and $A_j \leq 0.0064$.

The calculated values for the adsorption parameters under various operation conditions are summarized in Table 3, and the above rules are satisfied.

The reaction rate constant k for the Langmuir–Hinshelwood rate expression is:

$$k = (\frac{F^{inlet}_{CH_4}}{w_{cat}}) \cdot \int_0^{x_{CH_4}} \frac{(1 + K_{CH_4}p_{CH_4} + K_{H_2O}p_{H_2O}/p_{H_2})^2}{p^a_{CH_4} \cdot p^b_{H_2O} \cdot p^c_{H_2}(1 - \frac{p_{CO} \cdot p^3_{H_2}}{K_{eq,msr} \cdot p_{CH_4} \cdot p_{H_2O}})} \cdot dX_{CH_4} \tag{29}$$

3.4. Optimization routines of the methane steam reforming reaction kinetic parameters

The reaction rate constant k is a function of temperature which can be also expressed by the Arrhenius equation:

$$k = k_0 \cdot \exp(-E_{a,MSR}/(RT)) \tag{30}$$

where k_0 is the pre-exponential factor, and $E_{a,MSR}$ is the activation energy for the MSR reaction in J/mol, R is the universal gas constant, 8.314 J/(mol K), and T is the reaction temperature in K. Since the MSR kinetic parameters do not depend on the fuel gas compositions, and can be obtained by optimization routines to get the smallest deviation of k [37,40]. The effect of temperature on k was evaluated by increasing the temperature stepwise, from 973 K to 1048 K. The data analysis and model evaluation process is summarized in Fig. 2.
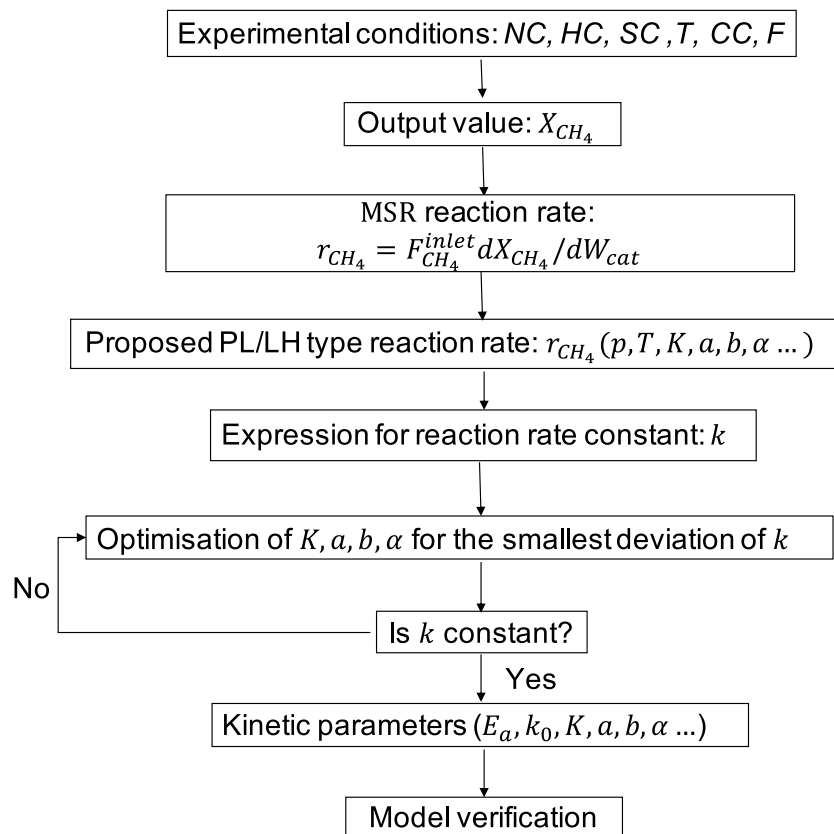
Experimental conditions: *NC, HC, SC ,T, CC, F*

Output value: X_{CH_4}

MSR reaction rate:
$$r_{CH_4} = F_{CH_4}^{inlet} dX_{CH_4}/dW_{cat}$$

Proposed PL/LH type reaction rate: $r_{CH_4}(p,T,K,a,b,\alpha\ ...)$

Expression for reaction rate constant: k

Optimisation of K, a, b, α for the smallest deviation of k

No

Is k constant?

Yes

Kinetic parameters $(E_a, k_0, K, a, b, \alpha\ ...)$

Model verification

Fig. 2. The data analysis process for the Power-Law and Langmuir–Hinshelwood kinetic models in the MATLAB script.

4. Results and discussion

The objective of this study is to get reliable reaction rate expressions for direct internal SOFCs at different operational conditions including current density and anode thicknesses. To do this, the influence of the operation conditions such as temperature, gas composition, current density and the anode thickness on the MSR reaction rate are investigated. In the first section, the influence of general operation conditions on the reaction rate were investigated. In the second and third sections, the influence of current density and anode thickness on the adsorption and kinetic parameters for both kinetic models are separately discussed. The specific MSR reaction rate under different operation conditions are listed in Table 4.

4.1. Influence of general operation conditions on the methane steam reforming reaction rate

Many groups have conducted experiments mostly on Ni-based catalysts in powder form or structured catalyst with different SC, NC and HC ratios at different temperatures with or without an external electrical loading. Different MSR reaction rates have been achieved with different units [18,29,31,41,55–58]. Nakagawa et al. [26] have reported that the catalytic activity could be influenced by the magnitude of the current density, and the steam and hydrogen partial pressures. Also, different electron densities, and different H^+ and O^{2-} concentrations might influence the reaction rate [1,59–62]. The previously reported MSR reaction rates are not comparable due to the very different test materials and conditions. In this section, we will mainly focus on the trend of the influence of the operation conditions on the reaction rates.

Table 4
Specific methane steam reforming reaction rates r_{CH_4} under different operation conditions. The temperature ranges from 973 K to 1048 K, and the current density varies from 0 to 1052 A/m².

Anode	Temperature, K	r_{CH_4}, ×10⁻³ mol/(min g)				
Thickness, µm	current density, A/m²	i	ii	iii	iv	v
A, 16 µm	973, 0	4.5	6.0	5.7	9.5	9.8
	973, 632	5.1	8.1	11.0	9.5	10.3
	973, 1052	5.3	8.5	11.1	10.0	10.7
	998, 0	5.0	7.1	7.9	10.8	11.3
	998, 632	6.5	9.6	13.0	11.5	11.7
	998, 1052	6.8	10.1	13.7	11.7	12.1
	1023, 0	6.0	8.6	11.6	11.9	12.6
	1023, 632	7.6	11.1	15.1	12.8	13.7
	1023, 1052	8.0	11.8	15.7	13.5	13.6
	1048, 0	6.6	11.4	15.7	13.3	13.8
	1048, 632	8.4	12.3	16.7	14.1	15.4
	1048, 1052	8.7	12.9	19.5	14.9	15.2
B, 27 µm	973, 0	2.6	4.9	6.2	5.2	5.2
	973, 632	4.3	6.4	8.9	6.6	7.1
	9738, 1052	4.6	6.6	8.6	7.1	6.0
	1023, 0	3.5	6.2	7.4	5.9	5.9
	1023, 632	4.8	7.4	10.1	7.5	7.9
	1023, 1052	5.1	7.5	10.2	7.9	7.8
	1048, 0	4.8	6.8	8.5	6.6	6.7
	1048, 632	5.6	8.4	11.6	8.6	9.1
	1048, 1052	5.9	8.9	11.7	8.8	8.6

4.1.1. Fuel gas composition

The influence of the fuel gas composition on the MSR reaction rate is shown in Fig. 3. A negative impact of steam partial pressure on the MSR reaction was observed. Increasing methane partial pressure can
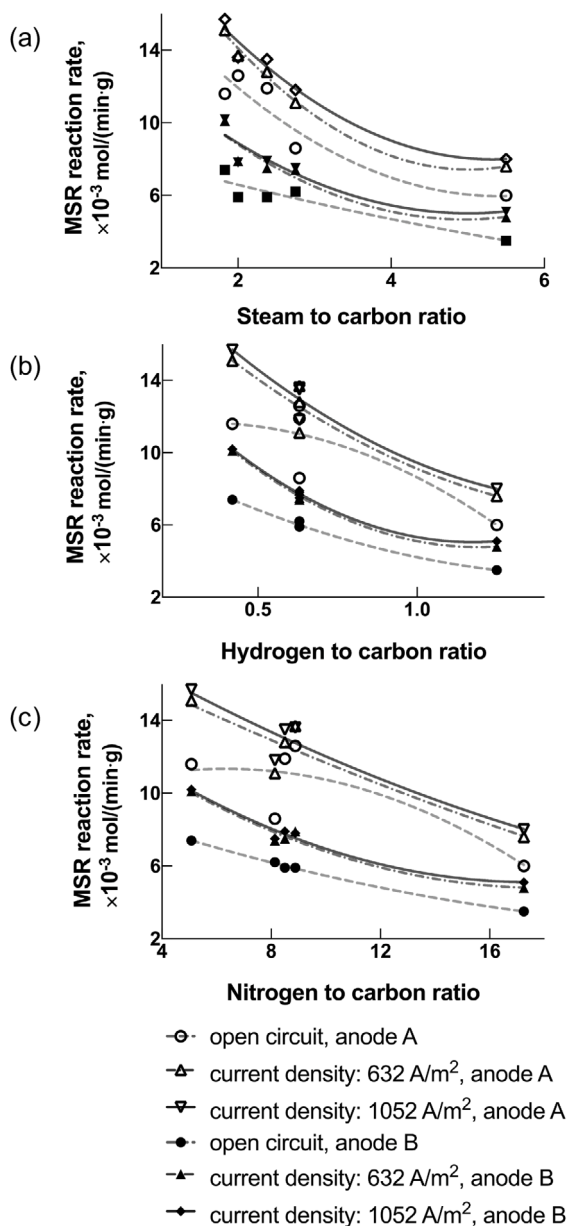
(a)

(b)

(c)

- -○- open circuit, anode A
- -△- current density: 632 A/m², anode A
- -▽- current density: 1052 A/m², anode A
- -●- open circuit, anode B
- -▲- current density: 632 A/m², anode B
- -◆- current density: 1052 A/m², anode B

Fig. 3. Influence of fuel gas compositions: (a) steam to carbon ratio (b) hydrogen to carbon ratio (c) nitrogen to carbon ratio on the methane steam reforming reaction rate at 1023 K. The current density varies from 0 to 1052 A/m², and the thickness is 16 μm for anode A and 27 μm for anode B.

- -○- open circuit, anode A, 16 μm
- -△- 632 A/m², anode A, 16 μm
- -◇- 1052 A/m², anode A, 16 μm
- -■- open circuit, anode B, 27 μm
- -▲- 632 A/m², anode B, 27 μm
- -▼- 1052 A/m², anode B, 27 μm

Fig. 4. Influence of the current density and anode thickness on the methane steam reforming reaction rate with inlet gas composition ii. The temperature ranges from 973 K to 1048 K, and the current density varies from 0 to 1052 A/m². The thickness is 16 μm for anode A and 27 μm for anode B.

reasons for these are similar to that of the influence of SC ratio. In addition to that, the increase of HC ratio shifts the reforming reaction equilibrium towards the left which is reflected by the decrease of the MSR reaction rate. This implies the possible competition among the methane, steam and hydrogen molecules on the catalytic sites of the catalyst surface which has been previously observed by Dicks et al. [63]. The main role of nitrogen in this study is to simulate a more realistic biosyngas composition for the SOFC as well as to keep the total inlet flow-rate constant for the purpose of scientific comparison. Different from the influences of the SC and HC ratios, the influence of NC ratio on the reaction rate mainly results from the dilution effect which can be seen from the smaller slopes of the fitted curves in Fig. 3(c). These above mentioned observations indicate the importance of the fuel compositions to the high-performance operation of direct internal reforming SOFC systems.

4.1.2. Temperature

The influence of the operating temperature on the reaction rate for the inlet gas composition ii is shown in Fig. 4. The MSR reaction rates increase with temperature for both anodes with various current densities. This is in good agreement with previously reported results [1,22,27,28]. A double increase of the reaction rate has been observed with a temperature increase of 75 K, compared with the results reported by Hou et al. in which with a temperature increase of 75 K, a quadruple increase of the reaction rate has been observed with a SC ratio of 4 [22]. The difference may be due to the different temperature ranges and the different catalytic materials. However, the effect is more evident than the results reported by Thallam Thattai et al. in which a maximum reaction rate increase of 10% observed with a temperature increase of 60 K. The temperature range used in their study was higher, and the SC ratio was lower compared with this study [28]. In Fig. 4, the trend could be also seen from the fitted curves for the closed-circuit cases where the temperature is relatively high, the influence of temperature on the reaction rate is slightly more significant compared with the lower temperature region. However, the trend is not reflected by all the fitted curves.

promote the MSR reaction as confirmed by many researchers [1,22,27, 28]. This implies the adsorption competition between the methane and steam molecules on the catalytic sites. However, the trend was steeper when the SC ratio is low, and gradually becomes flatter when the SC ratio further increases as shown in Fig. 3(a), especially under closed-circuit operation conditions. This result is also in good agreement with the results reported by Hou et al. and Thallam Thattai et al. [22,28]. The potential reasons are: (1) the increase of steam partial pressure decreases the methane partial pressure for a constant total reaction pressure; (2) the high steam partial pressure hinders the methane adsorption on the surface of the catalyst. Very similar to the influence of SC ratio, the influence of HC ratio was also steeper when the HC ratio is low, and gradually becomes flatter when the ratio is higher as shown in Fig. 3(b), especially under closed-circuit operations. This is also in good agreement with the results reported by Thallam Thattai [28]. The
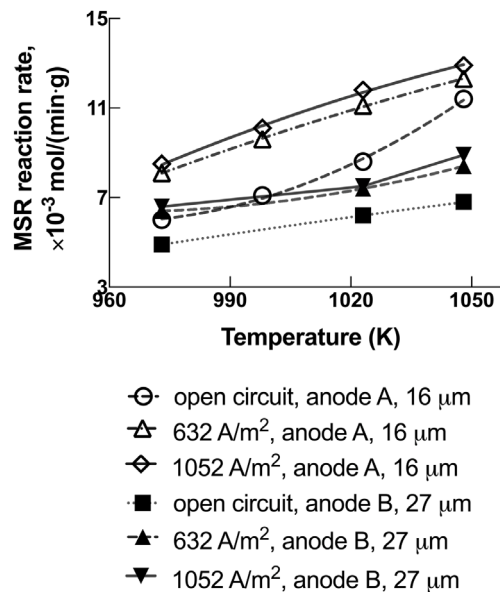
Table 5

Methane steam reforming kinetic parameters for the Power-Law kinetic model under various operation conditions. The temperature ranges from 973 K to 1048 K, and the current density varies from 0 to 1052 A/m^2.

Anode A, 16 μm Current density [A/m^2]	α_{CH_4}	α_{H_2O}	E_a [kJ/mol]	k_0
0	0.50	−1.19	59.27	5.38 mol/(min g bar$^{0.69}$)
632	0.56	−0.59	50.35	7.43 mol/(min g bar$^{0.03}$)
1052	0.59	−0.49	53.60	14.29 mol/(min g bar$^{-0.10}$)
Anode B, 27 μm Current density [A/m^2]	α_{CH_4}	α_{H_2O}	E_a [kJ/mol]	k_0
0	0.60	−0.02	56.17	23.20 mol/(min g bar$^{-0.58}$)
632	0.61	−0.14	31.46	1.33 mol/(min g bar$^{-0.47}$)
1052	0.58	0.11	35.75	3.11 mol/(min g bar$^{-0.69}$)

4.1.3. Current density

The MSR reaction rate increases significantly when drawing a current, and does not change significantly as the current density increases further, as shown in Fig. 4. The electrochemical reaction does not apply any dilution effect on the methane partial pressure. The influence is then due to the consumption of hydrogen which shifts the MSR reaction equilibrium towards a higher conversion which is reflected by a higher MSR reaction rate. In addition, it is believed that the MSR reaction rate is promoted by the O^{-2} ion flux at the TPB [22,64]. Similar effects have been also reported on Ni − GDC anodes [27,28,63,64]. On the other hand, the adsorption competition between the methane and steam molecules will hinder the further increase of the MSR reaction rate due to the extra generation of the steam from the electrochemical reaction. This explains why the MSR reaction rate does not further increase with a higher current density.

4.1.4. Anode thickness

The geometric areas of both anodes are the same, and assuming constant porosity, surface area, material composition, the amount of the active catalytic sites then only depends on the anode thickness. In an open-circuit SOFC, r_{CH_4} ($\times 10^{-3}$ mol/(min g)) on anode A is higher than that on anode B as shown in Table 4. This means the increase of anode thickness may not always bring in a higher reaction rate. r_{CH_4} for inlet composition ii on both anodes have been plotted in Fig. 4. On anode A, the difference between open-circuit and closed-circuit operations is smaller at a higher temperature; while on anode B, the difference between the reaction rates between open-circuit and closed-circuit operations are almost the same. The different effects of temperature may be due to the different responses of reaction rate coefficient and mass transfer coefficient to temperature on these two anodes [18,53].

4.2. Kinetic parameters in Power-Law model

The kinetic study has been conducted by analyzing the experimental results using data fitting. The values for the reaction orders, activation energy and the pre-exponential factor for the Power-Law kinetic model were calculated and listed in Table 5.

4.2.1. Influence of electrochemical reaction and anode thickness on Power-Law reforming kinetic parameters

The influence of the electrochemical reaction and anode thickness on the Power-Law kinetic parameters including the activation energy and reaction orders is shown in Fig. 5. The values for the calculated activation energy are within the previously reported range, and very close to the reported results by Belyaev et al. and Bebelis et al. [10,18, 21,27–29,35–38,40,55]. In Fig. 5(a). a minor decrease in the activation energy with current density is observed on anode A. On anode B, the values of the activation energy decrease significantly with a small
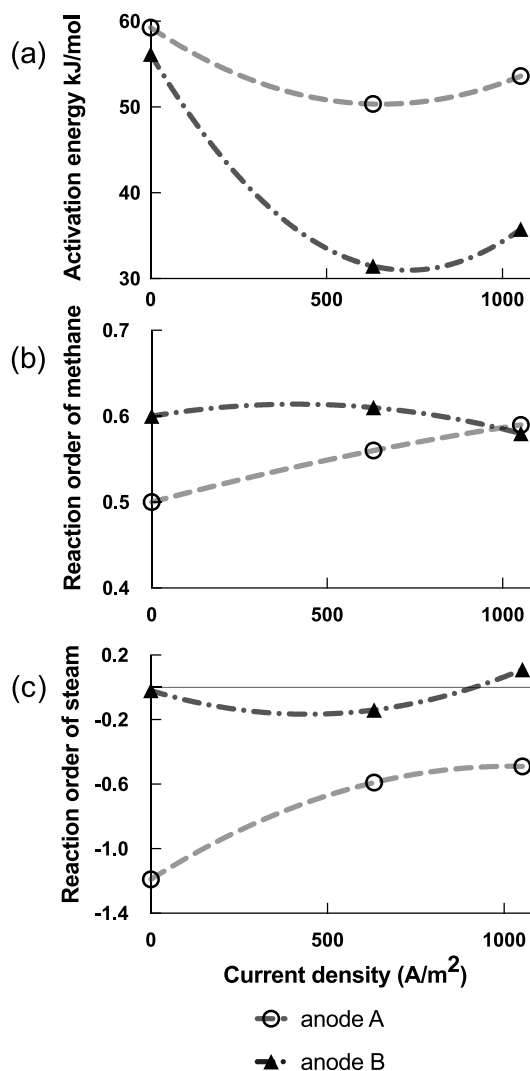

Fig. 5. Influence of the current density and the anode thickness on the (a) activation energy (b) methane reaction order and (c) steam reaction order in Power-Law kinetic model. The temperature ranges from 973 K to 1048 K, and the current density varies from 0 to 1052 A/m^2. The thickness is 16 μm for anode A and 27 μm for anode B.

current density. This might be explained by the existence of O^{2-} ion, an intermediate product from the surface dissociation of adsorbed steam molecules at the TPB that mitigates the negative influence of steam partial pressure on the MSR reaction [1,41,61]. Dicks et al. have reported the influence of current density on the MSR reaction rate that even a small current will affect significantly the local concentration of O^{2-} produced at the TPB, however the exact reasons were not further discussed [63]. The activation energy slightly increase with a higher current density on both anodes. A deterioration has been also observed with a higher current density on a Ni − YSZ − CeO$_2$ anode by Nakagawa et al. [26]. The reason why the changes are different on two anodes may be due to the anode thickness. Therefore, the anode thickness may play a significant role in direct internal reforming SOFCs when a current is produced.

The values for the reaction order of methane α_{CH_4} are smaller compared with the previously reported results ranging from 0.8 to 1.5 [18,26,27,29,38,40,41]. However, Thallam Thattai et al. has reported a value of 0.15 on a Ni-GDC anode in a complete SOFC and Mogensen et al. have reported a value of 0.56-0.8 on a Ni-YSZ anode [28,65]. In Fig. 5(b), the influence of the electrochemical reaction on α_{CH_4} is positive on anode A while the influence is slightly negative

on anode B. The values for α_{CH_4} become very close with a higher current density on two anodes which means a constant value of α_{CH_4} can be assumed in direct internal reforming SOFCs when Pow-Law rate expressions are used. The values for the reaction order of steam α_{H_2O} are mostly negative and comparable to the previously reported results ranging from −1.25 to 0.1 [18,26–29,37,38,40,41,65]. In Fig. 5(c), α_{H_2O} increases with current density on both anodes which might be due to the O^{2-} flux absorbed on the anode influencing the dependence of steam partial pressure [1,22,61]. This also implies that the dependence of the steam partial pressure is more complex compared with that of the methane partial pressure which has been previously observed in SOFCs when a current is drawn [27,28,34,65].

4.3. Kinetic parameters in Langmuir–Hinshelwood model

A mechanism study by Lee et al. suggested that the MSR reaction on Ni cermets follows a similar mechanism to conventional catalysts [35]. The measured MSR reaction rates reflect the intrinsic kinetics when the mass transfer effects are absent. The Langmuir–Hinshelwood kinetic model assumes a rate-determining step among the associatively adsorbed methane, steam and hydrogen [1,28]. The existence of a dependence of the product partial pressure is also considered because the product gas chemisorption may interfere with methane chemisorption by occupying the active surface sites. Therefore, the selected rate equation (Eq. (25)) can accommodate all the experimental observations. The hydrogen-dependent effect on the reaction rate is a consequence of the p_{H_2O}/p_{H_2} term in both the numerator and denominator. It is temperature dependent since the term is multiplied by k and K_{H_2O}, both of which are temperature-dependent. The values of the adsorption parameters for the Langmuir–Hinshelwood kinetic model are list in Table 3.

4.3.1. Influence of electrochemical reaction and anode thickness on the adsorption parameters

Catalytic MSR reaction consists of a series of elementary reactions: (1) reactants adsorption on the catalyst surface with or without dissociation occurs; (2) surface reactions occur; (3) and desorption of products occurs. In general, there are one or more slower steps, which control the overall rate of MSR reaction [1,20,22,61]. The adsorption isotherm for methane have been assumed not to be influenced by the current density and anode thickness which is reasonable given the fact that methane is mostly adsorbed on the surface of the catalyst [1,25,41,55,66]. The steam adsorption isotherm is more sensitive to the current density and anode thickness since steam absorption on the anode is not only from the anode surface but also could be from the triple-phase boundary when current is produced. Hence, the steam adsorption isotherm could vary with anode thickness and current density. The knowledge on spatial variations on chemical and electrochemical reactions within SOFC anodes is still developing, and hopefully the assumption is probably a step in the right direction but further study is certainly required.

The impact of the current density and anode thickness on the Langmuir–Hinshelwood adsorption constant K_{H_2O} is shown in Fig. 6. The values of the adsorption constant decreases with current on anode A while K_{H_2O} increases with current on anode B indicating the influence of the current are different on these two anodes. However, the adsorption constants with a higher current density are almost equal on both anodes implying the role of the anode thickness may vanish with a higher current.

K_{H_2O} depends on A_{H_2O} and $\triangle H^0_{H_2O}$ as shown in Eq. (26). It can be easily observed that the values of $\triangle H^0_{H_2O}$ are similar on both anodes under open-circuit operations as shown in Fig. 7(a). $\triangle H^0_{H_2O}$ decrease with a small current density and increase with a higher current density on both anodes. The trend also implies that $\triangle H^0_{H_2O}$ may become independent of the anode thickness with a higher current density. The influence of the electrochemical reaction on A_{H_2O} is shown in Fig. 7(b), and the frequency of the adsorption decrease with a small
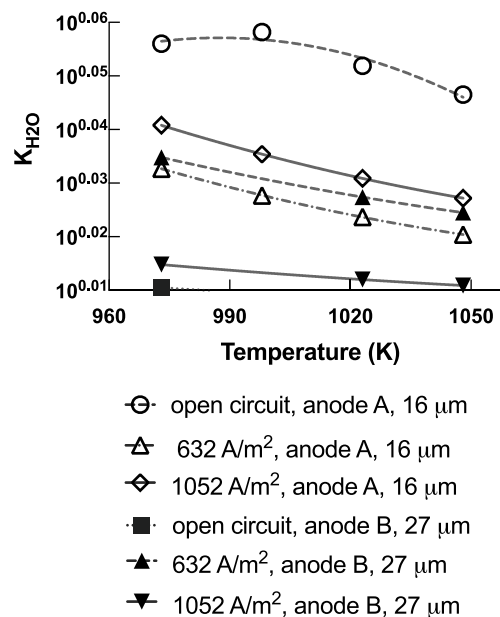
Fig. 6. Influence of the current density and the anode thickness on the steam adsorption constant in Langmuir–Hinshelwood kinetic model. The temperature ranges from 973 K to 1048 K, and the current density varies from 0 to 1052 A/m². The thickness is 16 μm for anode A and 27 μm for anode B.

current density significantly and increase with a higher current density on anode A; while the frequency of the adsorption frequency slightly increase with current density on anode B. A_{H_2O} may also become the same with a higher current density on both anodes. The influence of the electrochemical reaction on $\triangle S^0_{H_2O}$ is shown in Fig. 7(c). Similar to that of $\triangle A^0_{H_2O}$ and $\triangle H^0_{H_2O}$, a single value for $\triangle S^0_{H_2O}$ on both anodes is possible with a higher current density. The different responses from $\triangle H^0_{H_2O}$, A_{H_2O} and $\triangle S^0_{H_2O}$ are very likely due to different anode thicknesses which means the influence of the electrochemical reaction on anode A is more significant than that on anode B due to the higher O^{2-} concentration on the thinner anode given the same current density. However, the exact reason needs to be further studied, and a wider range of current density is highly recommended.

4.3.2. Influence of electrochemical reaction and anode thickness on the Langmuir–Hinshelwood reforming kinetic parameters

The values of the kinetic parameters for the Langmuir–Hinshelwood kinetic model are listed in Table 6.

The influence of the electrochemical reaction and anode thickness on the Langmuir–Hinshelwood kinetic parameters is shown in Fig. 8. The values for the calculated activation energy are smaller than most of the previously reported values for Langmuir–Hinshelwood kinetic model [1,28,29,38,41]. However, the values are very close to the reported results by Souentie et al. and Nakagawa et al. [26,34]. The values for the activation energy on these two anodes are very similar under open-circuit operation. The activation energy decreases with a small current density on both anodes as shown in Fig. 8(a). This could possibly also be explained by the existence of O^{2-} ion that mitigates the negative influence of steam partial pressure. The activation energy slightly increases with further increased current density on both anodes. Higher concentrations of steam molecules and O^{2-} ions accumulated at the TPB may cause Ni oxidation which could be reflected as a higher value of activation energy. Similar trend has been observed in the Power-Law kinetic model and a catalytic activity deterioration has been also observed with a higher current density on a $Ni-YSZ-CeO_2$ anode by Nakagawa et al. [26]. The influence of the electrochemical reaction on the activation energy is more significant

Table 6
Methane steam reforming kinetic parameters for the Langmuir–Hinshelwood kinetic model under various operation conditions. The temperature ranges from 973 K to 1048 K, and the current density varies from 0 to 1052 A/m^2.

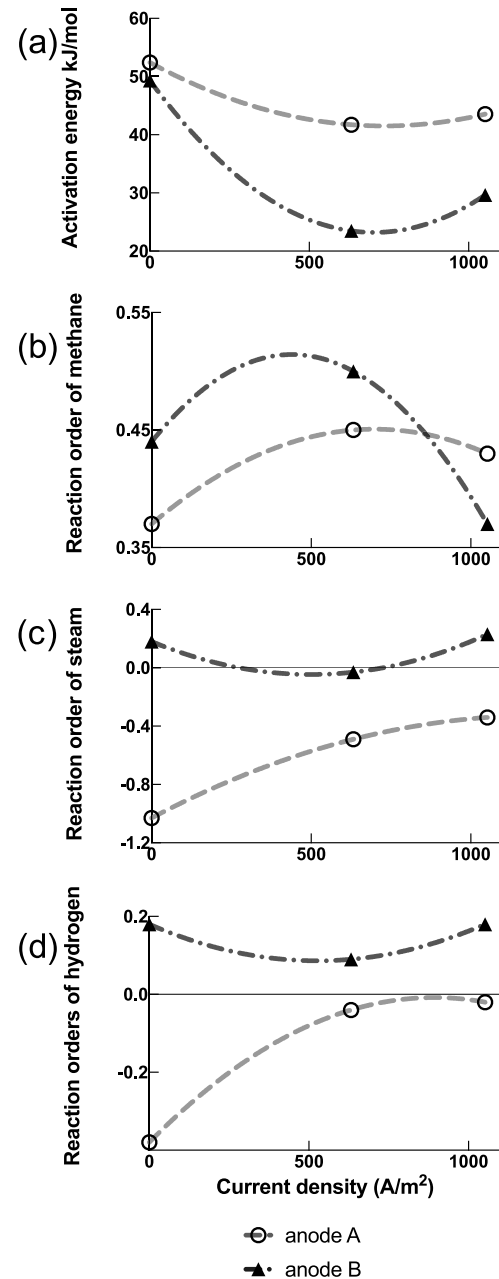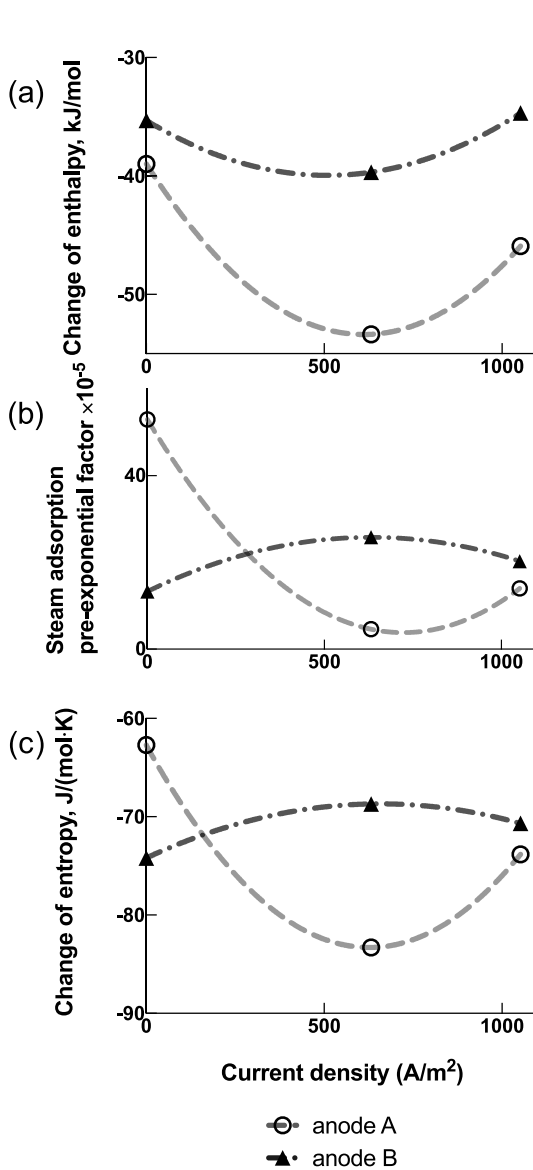| Anode A, 16 μm Current density [A/m^2]	a	b	c	E_a (kJ/mol)	k_0
0	0.37	−1.03	−0.38	52.43	1.10 mol/(min g bar$^{1.04}$)
632	0.45	−0.49	−0.04	41.73	2.37 mol/(min g bar$^{0.08}$)
1052	0.43	−0.34	−0.02	43.55	4.07 mol/(min g bar$^{−0.07}$)
Anode B, 27 μm Current density [A/m^2]	a	b	c	E_a (kJ/mol)	k_0
0	0.44	0.18	0.18	49.32	14.98 mol/(min g bar$^{0.80}$)
632	0.50	−0.03	0.09	23.48	1.08 mol/(min g bar$^{0.56}$)
1052	0.37	0.23	0.18	29.65	1.79 mol/(min g bar$^{0.78}$)

Fig. 7. Influence of the current density and the anode thickness on the steam adsorption parameters (a) change of enthalpy, (b) steam adsorption pre-exponential factor and (c) change of entropy in Langmuir–Hinshelwood kinetic model. The temperature ranges from 973 K to 1048 K, and the current density varies from 0 to 1052 A/m^2. The thickness is 16 μm for anode A and 27 μm for anode B.

Fig. 8. Influence of the current density and the anode thickness on (a) activation energy (b) methane (c) steam and (d) hydrogen reaction orders in Langmuir–Hinshelwood kinetic model. The temperature ranges from 973 K to 1048 K, and the current density varies from 0 to 1052 A/m^2. The thickness is 16 μm for anode A and 27 μm for anode B.

Table 7
Model evaluation using coefficient of determination R^2 and mean absolute percentage error, and model comparison using Akaike Information Criterion and Bayesian Information Criterion.

Parameter/Model	Power-Law	Langmuir–Hinshelwood
R^2	0.8537	0.9408
Mean absolute percentage error	8.92%	5.79%
Number of parameters	2	5
AIC	−2.79	−3.63
BIC	−2.77	−3.59

on anode B. Similar trends have been also observed in the Power-Law kinetic model which implies it may not be caused by the surface adsorption, but probably due to the different anode thicknesses.

The values for the reaction order of methane *a*, the reaction order of steam *b* and reaction order of hydrogen *c* are plotted against the current density in Fig. 8(b)–(d). *a* increases when a small current is drawn and decreases with a higher current density on both anodes. The values for *a* may become the same on both anodes when a higher current is drawn which implies that the dependence of the methane partial pressure may become independent of the anode thickness with a higher current density as shown in Fig. 8(b). The influence of the electrochemical reaction on *b*, shown in Fig. 8(c), is positive on anode A and non-uniform on anode B which may be because of the different O^{2-} concentrations at the TPB that influence the dependence of stream partial pressure differently due to different anode thicknesses. This also implies that the dependence of the steam partial pressure is more complex compared with methane. Same trends for *a* and *b* were also observed in the Power-Law kinetic model. The influence of the electrochemical reaction on *c* is shown in Fig. 8(d). Same trend has also been observed for *b*. This might be mainly due to the hydrogen consumption at the TPB which makes the dependence of hydrogen partial pressure on the reaction rate less significant, especially with a higher current density on anode A. The influence of current density on *b* and *c* are more significant and straight-forward on anode A due to the higher local concentrations of steam molecules and O^{2-} ions, and lower local concentration of hydrogen molecules on the thinner anode given the same current density. Similar non-uniform trends have also been reported by Thallam Thattai et al. [28].

4.4. Model evaluation and comparison

To better understand the difference between two kinetic models, we compared the Langmuir–Hinshelwood and the Power-Law models by considering the model performances in simulating the experimental reforming reaction rates under different operating conditions (see Table 7). The mean absolute percentage error between the simulated and experimental reforming reaction rate is smaller and the coefficient of determination R^2 is higher for the Langmuir–Hinshelwood kinetic model. While these evidences suggest that the Langmuir–Hinshelwood model produces a better quality of fit to the experimental data. We also acknowledge that the Langmuir–Hinshelwood model has more parameters compared to the Power-Law model. To account for the extra parameters in the model comparison, the Akaike Information Criterion (AIC) and the Bayesian Information Criterion (BIC) were used, both of which apply penalties to higher number of parameters Kassambara [67]. The result of this analysis reveals a lower AIC and BIC for the Langmuir–Hinshelwood kinetic model compared to the Power-Law kinetic model with a difference of 0.84 for AIC and 0.82 for BIC, further supporting that the Langmuir–Hinshelwood kinetic model describes the reaction rate better than the Power-Law kinetic model. However, it is worth noting that the number of experimental data are low, thereby limiting the accuracy of this analysis. Future work requires more experimental data to obtain a more comprehensive and reliable kinetic model for direct internal reforming SOFCs.

5. Conclusions

This study highlighted the influence of the electrochemical reaction and anode thickness on the MSR reaction rates and kinetics over two Ni–YSZ anodes. The Power-Law and Langmuir–Hinshelwood kinetic models were selected, and the following conclusions are drawn based on the observations and data analysis:

1. Steam to carbon ratio and hydrogen to carbon ratio both have a negative influence on the reforming reaction rate which is mainly due to the combination of the dilution effect to the methane partial pressure and the adsorption competition between steam/hydrogen and methane molecules on the catalytic sites.
2. The increase of the MSR reaction rate with a small current density may be because of the O^{-2} flux across the triple-phase boundary that promoted the MSR reaction. The adsorption competition between the methane and steam molecules will hinder the reaction which explains why the reaction rate does not further increase with a higher current density. Higher concentrations of steam molecules and O^{2-} ions accumulated at the TPB may cause Ni oxidation which could be reflected as a higher value of activation energy.
3. The influence of the current density on the reaction orders of methane and steam are similar in both models, and a constant value of the reaction order of methane may apply on both anodes when a high current is drawn.

This work helps formulate experimental work with appropriate kinetic models and provides convenient rate equations to the modeling study of the direct internal reforming solid oxide fuel cells. Future studies will take the effect of gas adsorption and mass-transport on the anode into account to elucidate the impact of anode thickness and electrochemical reaction on the reforming kinetics. More detailed experimental data should be provided for a better quality kinetic model.

CRediT authorship contribution statement

Liyuan Fan: Conceptualization, Methodology, Investigation, Data curation, Software, Writing – original draft, Project administration. **Anatoli Mokhov:** Data curation, Writing – review & editing. **S. Ali Saadabadi:** Methodology, Investigation, Writing – review & editing. **Nigel Brandon:** Writing – review & editing, Supervision, Funding acquisition. **Purushothaman Vellayani Aravind:** Supervision, Funding acquisition.

Declaration of competing interest

The authors declare that they have no known competing financial interests or personal relationships that could have appeared to influence the work reported in this paper.

Acknowledgments

Appendix A. Supplementary data

Supplementary material related to this article can be found online at https://doi.org/10.1016/j.jpowsour.2021.230276.

References

[1] J. Xu, G. Froment, Methane steam reforming, methanation and water gas shift: I. Intrinsic kinetics, AIChE J. 35 (1) (|1989|) 88–96.

[2] K. Eguchi, H. Kojo, T. Takeguchi, R. Kikuchi, K. Sasaki, Fuel flexibility in power generation by solid oxide fuel cells, Solid State Ion. 152 (|2002|) 411–416.

[3] J. Oueltjes, P. Aravind, N. Woudstra, G. Rietveld, Biosyngas utilization in solid oxide fuel cells with Ni-GDC anodes, J. Fuel Cell Sci. Technol. 3 (|2006|) 495.

[4] P. Aravind, W. de Jong, Evaluation of high temperature gas cleaning options for biomass gasification product gas for solid oxide fuel cells, Prog. Energy Combust. Sci. 38 (6) (|2012|) 737–764.

[5] P. Aravind, J. Oueltjes, E. de Heer, N. Woudstra, G. Rietveld, Impact of Biosyngas and its components on SOFC Anodes, Vol. 2005, Electrochemical Society Proceedings, |2005|, p. 7, Electrochemical Society Proceedings.

[6] L. Chen, Z. Qi, S. Zhang, J. Su, G.A. Somorjai, Catalytic hydrogen production from methane: A review on recent progress and prospect, Catalysts 10 (8) (2020) 858.

[7] S. Tsang, J. Claridge, M. Green, Recent advances in the conversion of methane to synthesis gas, Catalysis Today 23 (1) (1995) 3–15.

[8] F. Yu, T. Han, Z. Wang, Y. Xie, Y. Wu, Y. Jin, N. Yang, J. Xiao, S. Kawi, Recent progress in direct carbon solid oxide fuel cell: Advanced anode catalysts, diversified carbon fuels, and heat management, Int. J. Hydrogen Energy (2020).

[9] D. Papurello, S. Silvestri, S. Modena, Biogas trace compounds impact on high-temperature fuel cells short stack performance, Int. J. Hydrogen Energy 46 (12) (2021) 8792–8801.

[10] D. Mogensen, Methane steam reforming kinetics over Ni-YSZ anode materials for Solid Oxide Fuel Cells (Ph.D. thesis), |2011|.

[11] V. Somano, D. Ferrero, M. Santarelli, D. Papurello, CFD model for tubular SOFC directly fed by biomass, Int. J. Hydrogen Energy 46 (33) (2021) 17421–17434.

[12] V.M. Janardhanan, O. Deutschmann, CFD analysis of a solid oxide fuel cell with internal reforming: Coupled interactions of transport, heterogeneous catalysis and electrochemical processes, J. Power Sources 162 (2) (|2006|) 1192–1202.

[13] E. Vakoufts, G. Marnellos, C. Athanasiou, F. Coutelieris, CFD modeling of a biogas fuelled SOFC, Solid State Ion. 192 (1) (|2011|) 458–463.

[14] Q. Fu, Z. Li, W. Wei, F. Liu, X. Xu, Z. Liu, Performance degradation prediction of direct internal reforming solid oxide fuel cell due to Ni-particle coarsening in composite anode, Energy Convers. Manage. 233 (2021) 113902.

[15] L. Fan, Z. Qu, M. Pourquie, A. Verkooijen, P. Aravind, Computational studies for the evaluation of fuel flexibility in solid oxide fuel cells: A case with biosyngas, Fuel Cells 13 (3) (|2013|) 410–427.

[16] L. Fan, E. Dimitriou, M. Pourquie, M. Liu, A. Verkooijen, P. Aravind, Prediction of the performance of a solid oxide fuel cell fuelled with biosyngas: Influence of different steam-reforming reaction kinetic parameters, Int. J. Hydrogen Energy 38 (1) (|2013|) 510–524.

[17] A. Fernandes, T. Woudstra, A. Van Wijk, L. Verhoef, P. Aravind, Fuel cell electric vehicle as a power plant and SOFC as a natural gas reformer: An exergy analysis of different system designs, Appl. Energy 173 (2016) 13–28.

[18] E. Achenbach, E. Riensche, Methane/steam reforming kinetics for solid oxide fuel cells, J. Power Sources 52 (2) (|1994|) 283–288.

[19] J. Parsons, S. Randall, Experimental determination of kinetic rate data for sofc anodes, in: SOFC-Micromodelling IEA-SOFC-Task Report, 1992, pp. 43–46.

[20] S. Elnashaie, A. Adris, A. Al-Ubaid, M. Soliman, On the non-monotonic behaviour of methane-steam reforming kinetics, Chem. Eng. Sci. 45 (2) (1990) 491–501.

[21] V. Belyaev, T. Politova, O. Mar'ina, V. Sobyanin, Internal steam reforming of methane over Ni-based electrode in solid oxide fuel cells, Appl. Catalysis A: General 133 (1) (1995) 47–57.

[22] K. Hou, R. Hughes, The kinetics of methane steam reforming over a Ni-alpha-Al2O catalyst, Chem. Eng. J. 82 (1–3) (2001) 311–328.

[23] H. Zhu, R.J. Kee, V.M. Janardhanan, O. Deutschmann, D.G. Goodwin, Modeling elementary heterogeneous chemistry and electrochemistry in solid-oxide fuel cells, J. Electrochem. Soc. 152 (12) (2005) A2427.

[24] J. Wei, E. Iglesia, Isotopic and kinetic assessment of the mechanism of reactions of CH4 with CO2 or H2O to form synthesis gas and carbon on nickel catalysts, J. Catalysis 224 (2) (2004) 370–383.

[25] F. Minette, M. Lugo-Pimentel, D. Modroukas, A.W. Davis, R. Gill, M.J. Castaldi, J. De Wilde, Intrinsic kinetics of steam methane reforming on a thin, nanostructured and adherent Ni coating, Appl. Catal. B 238 (2018) 184–197.

[26] N. Nakagawa, H. Sagara, K. Kato, Catalytic activity of Ni-YSZ-CeO2 anode for the steam reforming of methane in a direct internal-reforming solid oxide fuel cell, J. Power Sources 92 (1–2) (|2001|) 88–94.

[27] L. Fan, L. van Biert, A.T. Thattai, A. Verkooijen, P. Aravind, Study of methane steam reforming kinetics in operating solid oxide fuel cells: Influence of current density, Int. J. Hydrogen Energy 40 (15) (2015) 5150–5159.

[28] A.T. Thattai, L. van Biert, P. Aravind, On direct internal methane steam reforming kinetics in operating solid oxide fuel cells with nickel-ceria anodes, J. Power Sources 370 (2017) 71–86.

[29] K. Ahmed, K. Foger, Kinetics of internal steam reforming of methane on Ni/YSZ-based anodes for solid oxide fuel cells, Catalysis Today 63 (2–4) (|2000|) 479–487.

[30] K. Eguchi, T. Setoguchi, T. Inoue, H. Arai, Electrical properties of ceria-based oxides and their application to solid oxide fuel cells, Solid State Ion. 52 (1–3) (|1992|) 165–172.

[31] J. Meusinger, E. Riensche, U. Stimming, Reforming of natural gas in solid oxide fuel cell systems, J. Power Sources 71 (1–2) (|1998|) 315–320.

[32] H. Zhu, W. Wang, R. Ran, Z. Shao, A new nickel-ceria composite for direct-methane solid oxide fuel cells, Int. J. Hydrogen Energy 38 (9) (|2013|) 3741–3749.

[33] D.L. King, J.J. Strohm, X. Wang, H.-S. Roh, C. Wang, Y.-H. Chin, Y. Wang, Y. Lin, R. Rozmiarek, P. Singh, Effect of nickel microstructure on methane steam-reforming activity of Ni–YSZ cermet anode catalyst, J. Catalysis 258 (2) (2008) 356–365.

[34] S. Souentie, M. Athanasiou, D. Niakolas, A. Katsaounis, S. Neophytides, C. Vayenas, Mathematical modeling of Ni/GDC and Au–Ni/GDC SOFC anodes performance under internal methane steam reforming conditions, J. Catalysis 306 (2013) 116–128.

[35] A. Lee, R. Zabransky, W. Huber, Internal reforming development for solid oxide fuel cells, Ind. Eng. Chem. Res. 29 (5) (|1990|) 766–773.

[36] H. Timmermann, D. Fouquet, A. Weber, E. Iverse Tiffee, U. Hennings, R. Reimert, Internal reforming of methane at Ni/YSZ and Ni/CGO SOFC cermet anodes, Fuel Cells 6 (34) (|2006|) 307–313.

[37] G. Brus, Y. Komatsu, S. Kimijima, J. Szmyd, An analysis of biogas reforming process on Ni/YSZ and Ni/SDC catalysts, Int. J. Thermodyn. 15 (1) (|2012|) 43–51.

[38] L. Van Biert, K. Visser, P. Aravind, Intrinsic methane steam reforming kinetics on nickel-ceria solid oxide fuel cell anodes, J. Power Sources 443 (2019) 227261.

[39] D. Mogensen, J.-D. Grunwaldt, P.V. Hendriksen, J.U. Nielsen, K. Dam-Johansen, Methane steam reforming over an Ni-YSZ solid oxide fuel cell anode in stack configuration, J. Chem. 2014 (2014).

[40] A. Sciazko, Y. Komatsu, G. Brus, S. Kimijima, J.S. Szmyd, A novel approach to the experimental study on methane/steam reforming kinetics using the orthogonal least squares method, J. Power Sources 262 (2014) 245–254.

[41] A. Dicks, K. Pointon, A. Siddle, Intrinsic reaction kinetics of methane steam reforming on a nickel/zirconia anode, J. Power Sources 86 (1–2) (|2000|) 523–530.

[42] W. Lehnert, J. Meusinger, F. Thom, Modelling of gas transport phenomena in SOFC anodes, J. Power Sources 87 (1) (|2000|) 57–63.

[43] L. Van Biert, M. Godjevac, K. Visser, P. Aravind, Dynamic modelling of a direct internal reforming solid oxide fuel cell stack based on single cell experiments, Appl. Energy 250 (2019) 976–990.

[44] V.M. Janardhanan, O. Deutschmann, CFD Analysis of a solid oxide fuel cell with internal reforming: Coupled interactions of transport, heterogeneous catalysis and electrochemical processes, J. Power Sources 162 (2) (|2006|) 1192–1202.

[45] Z. Qu, P. Aravind, N. Dekker, A. Janssen, N. Woudstra, A. Verkooijen, Three-dimensional thermo-fluid and electrochemical modeling of anode-supported planar solid oxide fuel cell, J. Power Sources 195 (23) (|2010|) 7787–7795.

[46] K. Girona, J. Toyir, P. Gelin, Y. Bultel, Modeling of a SOFC fuelled by methane: Influence of the methane steam reforming kinetics, ECS Trans. 35 (1) (|2011|) 945–954.

[47] H. Zhu, R.J. Kee, V.M. Janardhanan, O. Deutschmann, D.G. Goodwin, Modeling elementary heterogeneous chemistry and electrochemistry in solid-oxide fuel cells, J. Electrochem. Soc. 152 (12) (|2005|) A2427–A2440.

[48] R. Suwanwarangkul, E. Croiset, E. Entchev, S. Charojrochkul, M. Pritzker, M. Fowler, P. Douglas, S. Chewathanakup, H. Mahaudom, Experimental and modeling study of solid oxide fuel cell operating with syngas fuel, J. Power Sources 161 (1) (|2006|) 308–322.

[49] K. Nikooyeh, A.A. Jeje, J.M. Hill, 3D modeling of anode-supported planar SOFC with internal reforming of methane, J. Power Sources 171 (2) (|2007|) 601–609.

[50] G. Pekridis, K. Kalimeri, N. Kaklidis, E. Vakouftsi, E. Iliopoulou, C. Athanasiou, G. Marnellos, Study of the reverse water gas shift (RWGS) reaction over pt in a solid oxide fuel cell (SOFC) operating under open and closed-circuit conditions, Catalysis Today 127 (1–4) (|2007|) 337–346.

[51] D. Grenoble, M. Estadt, D. Ollis, The chemistry and catalysis of the water gas shift reaction: 1. The kinetics over supported metal catalysts, J. Catalysis 67 (1) (|1981|) 90–102.

[52] D. Mendes, A. Mendes, L. Madeira, A. Iulianelli, J. Sousa, A. Basile, The water-gas shift reaction: from conventional catalytic systems to pd-based membrane reactors-a review, Asia-Pacific J. Chem. Eng. 5 (1) (2010) 111–137.

[53] G.F. Froment, K.B. Bischoff, J. De Wilde, Chemical Reactor Analysis and Design, Vol. 2, Wiley New York, 1990.

[54] Z. Qu, P. Aravind, S. Boksteen, N. Dekker, A. Janssen, N. Woudstra, A. Verkooijen, Three-dimensional computational fluid dynamics modeling of anode-supported planar SOFC, Int. J. Hydrogen Energy 36 (16) (|2011|) 10209–10220.

[55] S. Bebelis, A. Zeritis, C. Tiropani, S. Neophytides, Intrinsic kinetics of the internal steam reforming of CH4 over a Ni-YSZ-cermet catalyst-electrode, Ind. Eng. Chem. Res. 39 (12) (|2000|) 4920–4927.

[56] P. Aguiar, C. Adjiman, N. Brandon, Anode-supported intermediate temperature direct internal reforming solid oxide fuel cell. I: model-based steady-state performance, J. Power Sources 138 (1–2) (|2004|) 120–136.

[57] W. Akers, D. Camp, Kinetics of the methane steam reaction, AIChE J. 1 (4) (|1955|) 471–475.

[58] D. King, J. Strohm, X. Wang, H. Roh, C. Wang, Y. Chin, Y. Wang, Y. Lin, R. Rozmiarek, P. Singh, Effect of nickel microstructure on methane steam-reforming activity of Ni-YSZ cermet anode catalyst, J. Catalysis 258 (2) (|2008|) 356–365.

[59] I. Fishtik, C. Callaghan, J. Fehribach, R. Datta, A reaction route graph analysis of the electrochemical hydrogen oxidation and evolution reactions, J. Electroanal. Soc. 576 (1) (|2005|) 57–63.

[60] I. Fishtik, C.A. Callaghan, R. Datta, Reaction route graphs. I. Theory and algorithm, J. Phys. Chem. B 108 (18) (|2004|) 5671–5682.

[61] G. Jones, J.G. Jakobsen, S.S. Shim, J. Kleis, M.P. Andersson, J. Rossmeisl, F. Abild-Pedersen, T. Bligaard, S. Helveg, B. Hinnemann, First principles calculations and experimental insight into methane steam reforming over transition metal catalysts, J. Catalysis 259 (1) (|2008|) 147–160.

[62] S. Clarke, A. Dicks, K. Pointon, T. Smith, A. Swann, Catalytic aspects of the steam reforming of hydrocarbons in internal reforming fuel cells, Catalysis Today 38 (4) (|1997|) 411–423.

[63] A. Dicks, Advances in catalysts for internal reforming in high temperature fuel cells, J. Power Sources 71 (1–2) (|1998|) 111–122.

[64] E. Ramırez-Cabrera, A. Atkinson, D. Chadwick, Catalytic steam reforming of methane over Ce0. 9Gd0. 1O2- x, Appl. Catal. B 47 (2) (2004) 127–131.

[65] D. Mogensen, Methane steam reforming kinetics over Ni-YSZ anode materials for solid oxide fuel cells, 2011.

[66] L. Maier, B. Schädel, K.H. Delgado, S. Tischer, O. Deutschmann, Steam reforming of methane over nickel: development of a multi-step surface reaction mechanism, Top. Catalysis 54 (13–15) (2011) 845.

[67] A. Kassambara, Machine Learning Essentials: Practical Guide in R, Sthda, 2018.